



Article

Numerical Simulation of the Lunar Polar Environment: Implications for Rover Exploration Challenge

Hong Gan ¹, Chengxuan Zhao ^{2,*}, Guangfei Wei ^{1,3,*}, Xiongyao Li ^{3,4}, Guojun Xia ^{1,5}, Xiao Zhang ^{1,5} and Jingjing Shi ¹

- ¹ Deep Space Exploration Laboratory, Hefei 230026, China; ganhong06@gmail.com (H.G.); xiaguojun90@163.com (G.X.); zxhit509@126.com (X.Z.); shijj0520@126.com (J.S.)
² Lanzhou Institute of Physics, China Academy of Space Technology, Lanzhou 730000, China
³ Center for Excellence in Comparative Planetology, Chinese Academy of Sciences, Hefei 230026, China; lixiongyao@vip.skleg.cn
⁴ Institute of Geochemistry, Chinese Academy of Sciences, Guiyang 550081, China
⁵ Shanghai Institute of Satellite Engineering, Shanghai 201109, China
* Correspondence: zhaocx2000@sina.com (C.Z.); gfwei0554@gmail.com (G.W.)

Abstract: The lunar polar regions are key areas for future exploration due to the long-term continuous illumination and persistently shadowed regions that can cold trap abundant water and other volatiles. However, the complex terrain, dynamic lighting, and solar wind-induced electric-field environment present multiple challenges for polar investigation and sampling missions. China's Chang'E-7 (CE-7) will explore the Moon's south polar region in 2026. One of the scientific goals is to drill samples in a wide area with a rover for in situ analysis. This study analyzes the engineering constraints of the polar illumination condition, slopes, and electric field for landing and sampling-site selection. Then, we create a 3D model of CE-7's lunar rover in three operating environments by employing the Spacecraft Plasma Interaction Software, with the rover sampling (i) on a flat surface, (ii) in a shadow, and (iii) near a meter-scale crater under different solar altitude angles. The results show that the rover can be charged to different potentials under the combined effects of solar wind incident angles and surrounding terrains. We find that a favorable traversing and/or sampling site of the rover for future polar exploration is in the upwind direction of a bulge (positively elevated terrains, such as the lander or boulders) or crater, which will cause a minimum charging effect on the rover. Our results have important implications for minimizing the risk of charging effects and guiding the lunar polar region exploration.

Keywords: lunar south pole; illumination condition; electric-field environment; Chang'E-7; lunar rover



Citation: Gan, H.; Zhao, C.; Wei, G.; Li, X.; Xia, G.; Zhang, X.; Shi, J. Numerical Simulation of the Lunar Polar Environment: Implications for Rover Exploration Challenge. *Aerospace* **2023**, *10*, 598. <https://doi.org/10.3390/aerospace10070598>

Academic Editor: Junyue Tang

Received: 11 April 2023

Revised: 25 June 2023

Accepted: 27 June 2023

Published: 30 June 2023



Copyright: © 2023 by the authors. Licensee MDPI, Basel, Switzerland. This article is an open access article distributed under the terms and conditions of the Creative Commons Attribution (CC BY) license (<https://creativecommons.org/licenses/by/4.0/>).

1. Introduction

The exploration of the lunar polar regions represents a fascinating prospect for future endeavors on the Moon due to the presence of abundant water resources and other volatiles [1–3] and its unique illumination condition [4–6]. Lunar near-surface materials including minerals, volatiles, and water ice are expected to be crucial for in situ resource utilization, such as lunar-base construction [7]. The Volatiles Investigation Polar Exploration Rover (VIPER), part of NASA's Artemis mission, is set to launch in late 2024 to explore water ice and other potential resources [8,9]. The rover powered by a solar-charged battery can detect and drill near-surface water ice for scientific analysis and as a resource for future human missions. The Lunar Polar Exploration Mission (LUPEX) is a joint robotic mission of the Japan Aerospace Exploration Agency (JAXA) and the Indian Space Research Organisation (ISRO) to explore the lunar south pole [10]. The rover will be provided by JAXA to prospect potential water and drill subsurface samples from a 1.5-m depth [11]. As part of the fourth phase of China's Lunar Exploration Program (CLEP), the Chang'E-7

(CE-7) mission will explore the Moon's southern polar region with a set of spacecraft elements [12]. The lunar rover equipped with a series of payloads and a sampling robotic arm is designed to investigate the sunlit surface in wide-area and longitudinal multi-point sampling modes [13].

The relatively small angle ($\sim 1.54^\circ$) between the Moon's equatorial plane and the ecliptic plane results in a solar altitude angle of only a few degrees at the lunar polar regions. Coupled with the rugged highland terrains containing abundant impact craters, extreme lighting conditions are created near the poles [3,4]. It is worth noting that the electric-field environment on the lunar surface is closely related to the illumination conditions. For example, the solar wind-induced electric field becomes complicated because the polar regions are always near the terminator [14]. Thus, a rover investigation including drilling samples will inevitably face a complex environment of nearly real-time dynamic illumination, electric field, and dust levitation during the mission [15]. Especially for the shadowed area, the surface is negatively charged due to the accumulation of electrons deposited from the solar wind. As a result, the negatively charged dust particles will be repelled from the surface that can be adhered to by the rover. This could abrade the optical lens and disable mechanical movement [16,17], which in turn would signify rover sampling mission failure.

Considering the ubiquitous craters on the Moon and the low solar altitude angle at the lunar polar regions, an obvious plasma wake structure within craters is formed [18]. Research has shown that the surface potential at the bottom of the Shackleton crater can reach a negative potential of several hundred volts due to the plasma wake effect [19]; that is, the electron-cloud region enhanced by a plasma dusty environment presents potential hazards for surface exploration within craters, which has been verified by five dust enhancement events near a twilight crater during the Lunar Atmosphere and Dust Environment Explorer (LADEE) mission [20]. The effect of the solar storm on the plasma wake [21] and the characteristics of the recursive mini-wake ("crater-in-a-crater" model) in the lunar polar crater [22] have been discussed. Furthermore, the boundary conditions along the plasma expansion front have also been analyzed [23]. Recently, Mishra described the electric potential distribution of the surface within permanently shadowed craters on the Moon [24].

However, the charging process in the sunlit area and its influence on the rover in the polar regions are less studied. The lunar dust detectors in the Chang'E-3 and 5 (CE-3/5) missions also detected levitated charged dust particles during the missions [25,26]. It is worth noting that the lunar-dust detectors were installed on the landers at heights of 1.9 m and 2.0 m, respectively. The landers were charged by solar wind plasma, further interacting with the surrounding plasma and affecting subsequent electrostatic dust migration. A similar phenomenon could also happen with rovers. In 2015, the Spacecraft Plasma Interactions Software (SPIS) developed by the European Space Agency was improved to simulate the lunar and asteroid dust emission, transport, deposition, and interaction with a spacecraft on or close to the lunar surface [27]. Using SPIS, Xia et al. (2022) discussed the effect of the varying solar altitude angle on the spatial distribution of dust and plasma above the lunar surface near a 5-m crater (in diameter) and verified the dust risk of spacesuits on the dayside and nightside [28].

Combined with the topography, we numerically simulated the illumination and electric-field environment in the lunar south polar region to clearly understand the environmental challenges faced by the rover. In this study, we first present the engineering constraints of slope, illumination, and electric field for polar landing-site selection in Section 2. In Section 3, we introduce the 3D simulation model and setup of parameters. Our results are given in Section 4, in which we present three situations of lunar rover charging at different solar altitude angles. In Section 5, we give a discussion of the study. Finally, a conclusion is given in Section 6.

2. Engineering Constraints

2.1. Complex Terrain

The polar regions of the Moon are characterized by complex terrains, such as the wide distributions of impact craters, steep walls, depressions, and ridges. Therefore, selecting a landing area that meets the constraints of terrain and scientific exploration objectives is crucial. Figure 1a shows the topography of the lunar south polar region ($>87^\circ$) with a spatial resolution of 20 m/pixel. The potential exploration target, the Shackleton crater, which lies close to the south pole, is a bowl-shaped crater with a diameter of 21 km and a depth of 4.2 km. Multiple lunar missions have indicated that water ice is exposed and/or buried within the permanently shadowed crater [2], which is considered a favorable exploration target of the CE-7 mission [13]. The crater rim and connecting ridges present a prominent high elevation within this polar region. The surface parameter, the slope, can be derived from the digital elevation model (DEM) data. The slope is an important parameter for landing-site selection and also a key factor for the rover's path planning. Figure 1b shows that the Shackleton crater presents a relatively steeper wall, with an average slope of 35° , but a relatively flat bottom. One prominent area characterized by high elevations but small slopes has been selected as our study area (dashed box of Figure 1a,b). The statistics of the histogram (Figure 1c) of the slope map within our study area show that the slope range is $0\text{--}45^\circ$ with an average slope of 17.4° . In addition, pixels with slopes of less than 25° account for a high percentage ($\sim 89.8\%$) of the whole area.

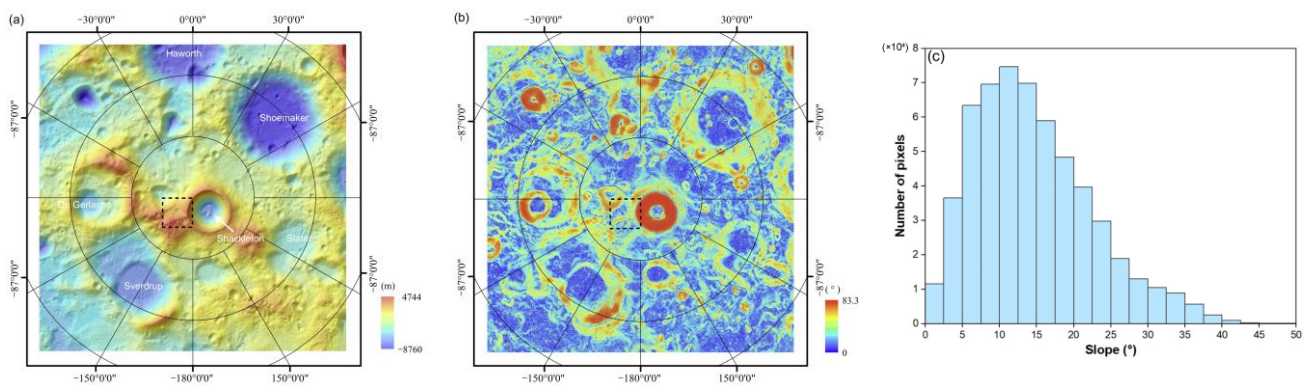


Figure 1. Topography (a) and slope distribution (b) of the lunar south pole ($>87^\circ$ S), and slope histogram (c) of the study area enclosed by the dashed box in (a,b).

2.2. Illumination Conditions

The study of water ice and other volatiles is the main scientific goal of the CE-7 mission; thus, this study takes the Shackleton crater as the potential target. Meanwhile, the strategy for the continuous operation of the rovers is to autonomously navigate to the sunlit areas under the constraints of engineering such as slope to ensure appropriate temperature and sufficient energy supply. A 15×15 km area near the south pole including a partial crater rim and connecting ridge (dashed box of Figure 1a,b) is investigated in detail. Based on the 20 m/pixel polar DEM data obtained from LRO LOLA, we modeled the real-time illumination conditions at the study area by employing the SPICE toolkit and horizon method [4]. Figure 2a shows the time-averaged illumination rate of 2026. Here, the illumination rate is defined as the ratio between the total illumination time of a place in a year and the total time of the year. Regions with illumination rates greater than 80% and slopes smaller than 10° are marked by green pixels. These regions are mainly located at the Shackleton crater rim and connecting ridges, which have a total area of $40,400 \text{ m}^2$. Note that these landing-of-interest regions are partially continuous, which requests a precise landing-site selection and traversing path planning. Figure 2b shows the histogram of the illumination rate in the study area. A majority of the pixels within the study area exhibit an illumination rate below 50%. The number of pixels decreases substantially with the increasing illumination rate.

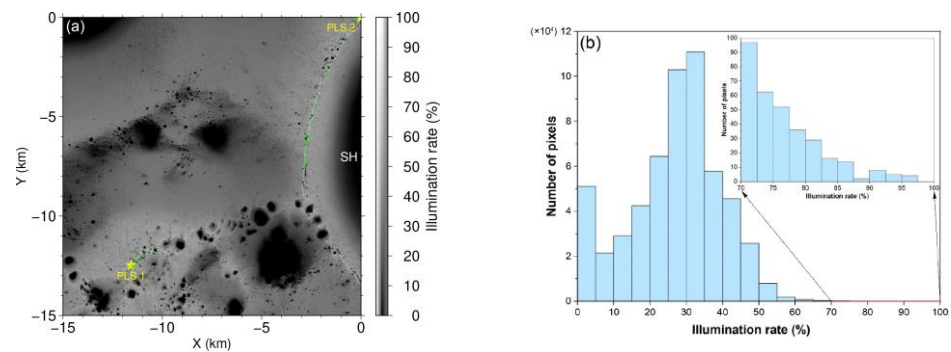


Figure 2. (a) Modeled illumination rate of 2026 within the study area. (b) Histogram of illumination rate. The green dots in (a) indicate areas with slopes less than 10° and illumination rates greater than 80%. Two potential landing sites, PLS 1 (137.14° W, 89.44° S) and PLS 2 (135.22° W, 90.00° S), are labeled by stars. SH denotes the Shackleton crater.

Considering the slope constraint for engineering safety, Figure 3 shows the total illumination area that varies as a function of the illumination rate under different slope constraints ($\leq 25^\circ$, $\leq 20^\circ$, $\leq 15^\circ$, $\leq 10^\circ$, $\leq 5^\circ$). For lower illumination rates of less than 70%, the constrained potential landing area is dependent upon the slope, especially for slopes in the range of 5° – 10° . For higher illumination rates of greater than 70%, the difference in the potential landing area constrained by different slopes can be neglected; that is, based on the 20 m/pixel scale DEM resolution, the selection of the potential landing site in the future will depend greatly on the lighting condition within this area.

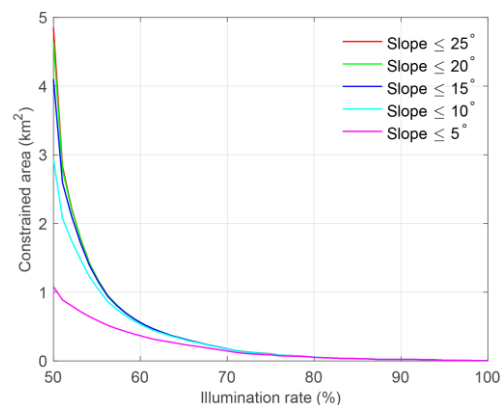


Figure 3. The total illuminated area varies as a function of the illumination rate under different slope constraints.

Once landing on the Moon, the local slope will play an important role in the thermal control system, energy supply, and optical imaging. Figure 4 shows the local solar altitude angle at two potential landing sites, PLS 1 (137.14° W, 89.44° S) and PLS 2 (135.22° W, 90.00° S), which have been marked in Figure 2a. As shown in Figure 4, PLS 2 (blue line) presents a larger variety of solar altitude angles than those of PLS 1 (red line) in 2026 because the local slope of PLS 2 (9.93°) is much larger than that of PLS 1 (1.01°). The maximum solar altitude angle at PLS 1 is $\sim 1.98^\circ$, while PLS 2 reaches an angle of $\sim 11.44^\circ$. This will cause about a 224-watt/m^2 difference at a 1-AU distance from the Sun. Additionally, the local solar altitude angle is larger in the southern summer (light red shade) than in winter (light blue shade). This will cause a ~ 23 and ~ 34 watts/m^2 difference for PSL 1 and PSL 2, respectively. It is worth noting that there are two continuous solar illumination periods at PLS 1: one from 20 January 2026 to 20 April 2026, and another from 25 October 2026 to 31 December 2026, which last more than 90 and 67 days in 2026, respectively. Thus, a place such as PLS 1 would be a favorite landing site for long-term polar exploration.

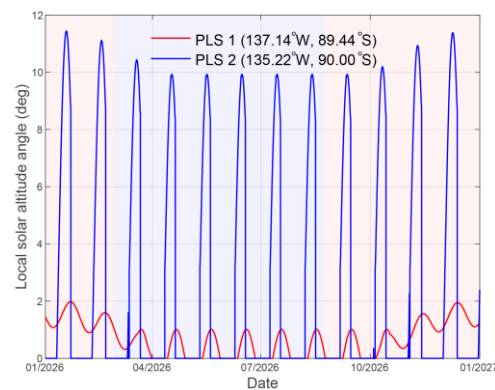


Figure 4. Variation in the solar altitude angle at PLS 1 ($x = -11,570$ m, $y = -12,470$ m) and PLS 2 ($x = -10$ m, $y = -10$ m) in 2026. The light red and blue shades denote southern summer and winter, respectively. Note that the local slopes of PLS 1 and PLS 2 are 1.98° and 9.93° , respectively.

2.3. Electric-Field Environment

The solar wind-induced electric field also plays an important role in the polar environment assessment and lunar-surface exploration/operation. Figure 5 shows the effective solar irradiance and surface potential within the study area. As a result of the nearly horizontal incidental sunlight, only part of the Shackleton crater rim and the connecting ridge between the Shackleton and de Gerlache craters are illuminated [29,30], where the solar irradiance is mainly below 300 watts/m², as shown in Figure 5a. In comparison, most of the study area is in the shadowed region.

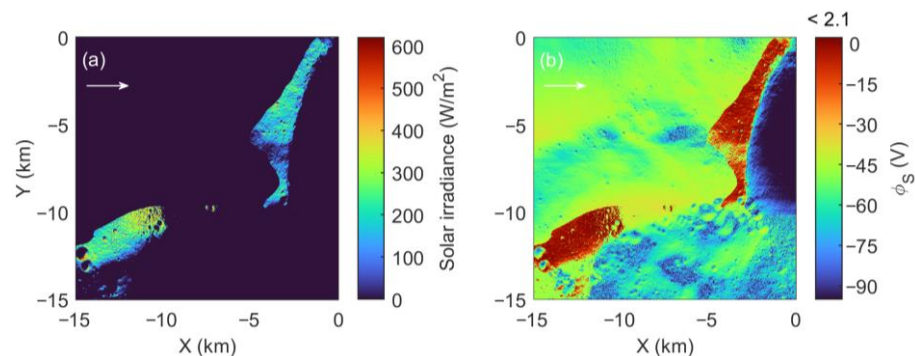


Figure 5. Distribution of the effective solar irradiance (a) and the surface potential (b) within the study area.

The surface potential of the illuminated area is from -15 to 2.1 V, as shown in Figure 5b. However, for the shadowed area, the surface is charged to a large range of negative potentials from -90 to -30 V. Except for the bottom of the Shackleton crater, the surface potential is concentrated in the range of -70 V to 0 . Bounded by the ridge between the Shackleton crater and the de Gerlache crater, the potential on the upper side is between -60 and -40 V, while the potential on the lower side can reach -70 V. This is because the shadowed region on the upper side formed by the shading of the edge of the de Gerlache crater is further away from the shielding edge.

The unilluminated ridge region between the Shackleton crater and the de Gerlache crater has a relatively higher potential between -45 and -35 V. Unlike solar energy utilization only in the sunlit area, the rover will face an inhomogeneous electric environment in the study region; that is, the rover interacts with the surrounding plasma and then could be charged to different states during traversing. Next, we will analyze how the rover changes the surrounding electric-field environment using SPIS.

3. Simulation Model

3.1. Model Setup of the Lunar Rover

We build a three-dimensional six-wheeled solar-powered lunar rover model with a length of 1.5 m, a width of 1.2 m, and a height of 1.0 m using SPIS (Figure 6). The rover body is coated by indium tin oxide (ITO) for thermal control. The upper surface of solar panel arrays with a unilateral width of 1.3 m is composed of cation-exchange resins (CERs), while the lower surface and side of the wings are composed of conductive fiber-reinforced polymer (CFRP). The wheels are designed to be composed of aluminum. The coupling resistance between the main body of the lunar rover and the solar array is set to 10 k Ω , the electrical connection is achieved between the wheels and the body, and the coupling resistance between the rover and the lunar surface is set to 1 k Ω . The simulation domain of the near-surface environment of the rover exploration is set to a region of 40 \times 40 \times 80 m in surface length, width, and height, which is divided by non-uniform grids. In our work, the stationary rover is charged by the solar wind, thereby the friction charging between the rover and lunar soil will be not considered. The lunar-surface material (i.e., dust) is set to be conductive when exposed to solar irradiation but to become non-conductive while in the shadow. The simulation period is set to 2000 s, ensuring the lunar surface reaches a quasi-equilibrium of charging.

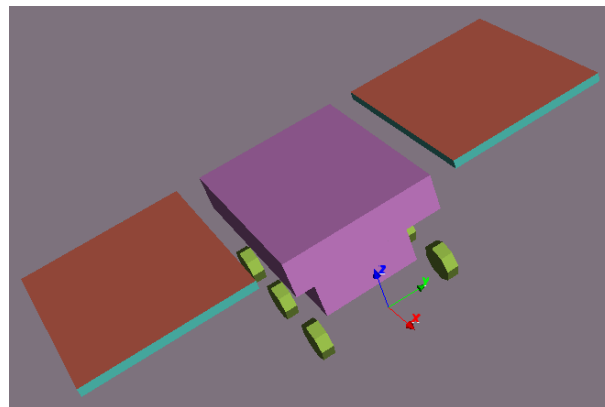


Figure 6. A 3D model of a lunar rover created by SPIS software (Version 5.2.4).

3.2. Setup of the Plasma Environment

The Moon revolves around the Earth and the Sun simultaneously. Therefore, it will encounter different complex plasma environments due to the solar wind and the Earth's magnetic field. The solar wind environment includes several types: coronal mass ejections (CMEs), high-speed streams, and slow solar wind. The Moon spends most of its time in the last environment. The fluxes of electrons and ions in the slow solar wind are much smaller than those during coronal mass ejections. Secondly, Earth's magnetotail extends well beyond the orbit of the Moon, so that the Moon has to face the magnetic environment, such as the magnetosheath environment, the high-latitude magnetotail lobe environment, and the plasma sheet environment, where solar wind plasma and charged dust particles could be deflected or oscillated by the Earth's magnetic field. This means that in the magnetic field, the direction of the plasma particles incident on the lunar surface is uncertain. Meanwhile, the electron and ion temperatures inside the Earth's geomagnetic tail are larger than those in the slow solar wind, while the electron and ion densities inside the geomagnetic tail are smaller than those in the slow solar wind. Therefore, the surface charging of the lunar rover inside the geomagnetic tail could be more serious and unpredictable [31], although the Moon stays in the Earth's magnetosphere for only about 6 days every month. Furthermore, due to the small tilt of the spin axis and cratered terrain, the small solar altitude angle in the polar region will create an extremely complex plasma charging environment, even under the typical slow solar wind condition. As a result, polar exploration missions such as CE-7 would face a more rigorous challenge. Hence, taking the slow solar wind environment as

an example, we set the simulated regional plasma environment. The slow solar wind has solar wind speeds below ~ 400 km/s and typically is relatively dense. Table 1 shows the parameter settings of the simulated slow solar wind environment.

Table 1. Environmental parameter setting of the slow solar wind at the Moon's south pole.

Parameters	Values	Unit
Solar wind ion density, n_i	10	cm^{-3}
Solar wind electron density, n_e	10	cm^{-3}
Ion velocity, V_i	400	$\text{km}\cdot\text{s}^{-1}$
Electron velocity, V_e	400	$\text{km}\cdot\text{s}^{-1}$
Ion temperature, T_i	8.6	eV
Electron temperature, T_e	12.1	eV
Photoelectron temperature, T_{ph}	2	eV
Solar altitude angle, θ_s	1 or 10	$^\circ$ (degree)
Dust mean radius, r_{avg}	10^{-6}	m

The lunar rover is exposed to the dusty plasma environment near the lunar surface. We suppose that the relevant charging currents at the local surface of the rover include currents of solar wind electrons (J_e), solar wind ions (J_i), photoelectrons (J_{ph}), and secondary electrons (J_{se}), as well as charged dust particles (J_d). The surface charging currents are regulated by the surface potential. When the surface charging reaches an equilibrium, the sum of all currents coming in equals the sum of all currents going out; that is, the surface potential makes the sum of all currents zero. Based on the above current-balance theory, the surface potentials of the rover and the local lunar surface are obtained.

4. Results

As mentioned above, a favorable landing site in polar regions should be constrained by a high illumination rate but a small slope. The rover's in situ investigation and sampling are powered by solar energy while the spacecraft is exposed to the high-incident solar wind. Considering the complex terrain of polar regions, here, we report and discuss three cases of simulation results in which the rover interacts with its surrounding environment.

4.1. Lunar Rover Charging on a Flat Surface

On the relatively flat lunar surface without shade from the surroundings, the charging process of the lunar rover is mainly controlled by the solar wind plasma and its incident angle, as shown in Figure 7. It can be seen that the solar wind plasma will form low potential regions on the windward side and the back side of the lunar rover when the solar altitude angle is 1° and 10° due to the topography. As shown in Figure 7a, for the lower solar altitude angle (1°), the surface potential of the entire area is -25 V. However, on the windward side of the rover, the surface potential can be as low as -27.6 V due to the accumulation of solar wind electrons and photoelectrons emitted by the ITO coating of the rover body. On the leeward side of the lunar rover, a low-potential area in a long-strip shape but wider than the rover is formed because the sunlight is shaded by the lunar rover and because the lunar regolith no longer emits photoelectrons. The surface potential of the solar wing reaches the highest value of -22.5 V, while the other parts of the rover including the carbon fiber structure of the solar cell array, the main body of the rover, and the wheels are a little lower at -24 V.

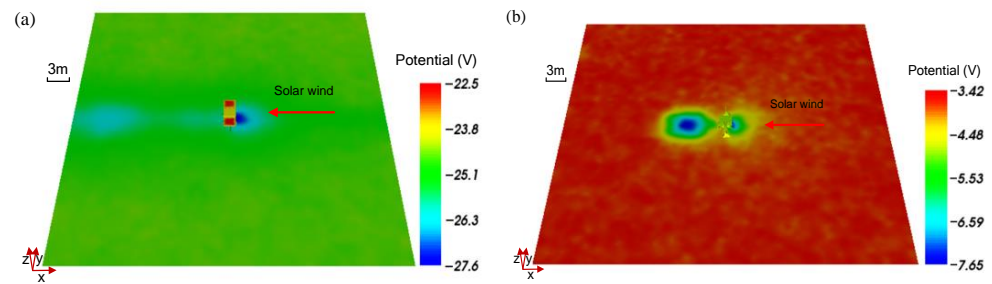


Figure 7. The charging potential of the lunar surface and the rover when the solar altitude angle is 1° (a) and 10° (b).

Compared to the 1° solar altitude angle, the charging process of the lunar surface at a 10° solar altitude angle is eased due to the increase in photoelectron density. As shown in Figure 7b, the surface potential increases to about -3.42 V. However, on the windward side of the rover, the surface potential is decreased to -7.0 V due mainly to the accumulation of photoelectrons emitted by the rover body. On the leeward side of the rover, a near-circular low-potential area slightly larger than the width of the rover is also formed. This area has a slightly reduced potential of -7.65 V as a result of the shadowing effect of the rover on the solar wind and the sunlight. Note that when the solar altitude angle is 1° or 10° , the shadow length is 57.3 or 5.7 m, respectively. Therefore, for the 10° solar altitude angle, the low-potential area follows the leeward side of the rover and adjoins it. When the solar altitude angle increases to a higher value, the solar array of the rover receives more irradiation and solar wind particles, which results in the glass cover of the solar wing and other conductive parts (carbon-fiber structure of the solar array, the main body of the rover, and the wheels) reaching a similar value of about -5.0 V.

For the plasma potential distribution in the entire simulation area, the potential at the upper boundary of the domain with a height of 80 m is zero for the solar altitude angles 1° and 10° (Figure 8). It is worth noting that the entire near lunar surface (5-m above the surface) is full of low-potential plasma when the solar altitude is 1° (Figure 8a). However, only relatively low-potential plasma remains around the rover when the solar altitude angle is 10° (Figure 8b).

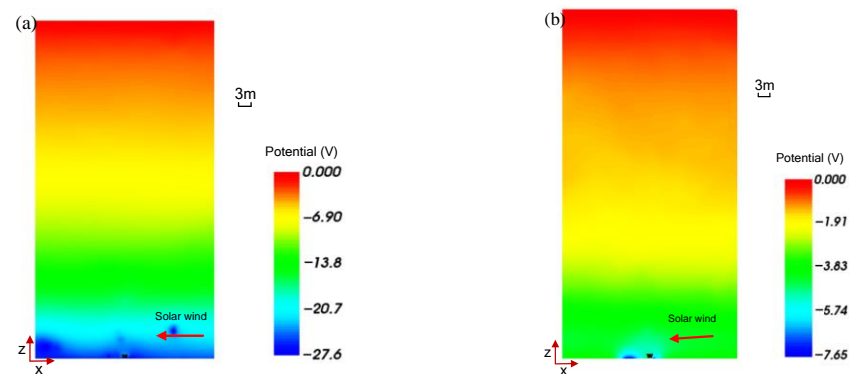


Figure 8. The plasma potential distribution in the simulated area with the solar altitude angle is 1° (a) and 10° (b).

4.2. Lunar Rover Charging in a Shadow

Considering the rover investigating and/or sampling near a lunar bulge, such as perched rocks, the characteristics of the local electric field might be influenced by the shadowing effect. As a result, this will affect the charging process of the rover. Here, assuming a 2-m high terrain at 4 m near the windward side of the rover, the charging potentials of the lunar surface and the rover can be simulated at different solar altitude angles. Figure 9 shows the simulated surface and rover charging shadowed by the bulge.

A greater number of electrons are deposited in the tail area to form a typical wake area, which causes surface charging, especially for the rover. For a lower solar altitude angle of 1° (Figure 9a), the surface is charged to a relatively high potential of -26.6 V due to the photoelectron effect. However, the shadowed area contains only deposited electrons which causes a lower surface potential with a long strip shape. In particular, the solar arrays of the rover that are composed of CERS can be charged to a very low potential of -63 V. Notably, a low potential area in the windward side of the bulge is also formed as a result of photoelectron deposition. We also simulated the surface charging when increasing the solar altitude angle to 10° (Figure 9b). Assuming the surface irradiated by the solar wind is a conductive area and the shadowed area is a non-conductive area, it can be seen that the surface is charged dramatically to a relatively high potential as a result of increased photoelectron emission. Thus, the surface potential rises to -10.4 V, while the shadowed area and lunar rover are charged to a lower potential with the highest negative potential of -45 V.

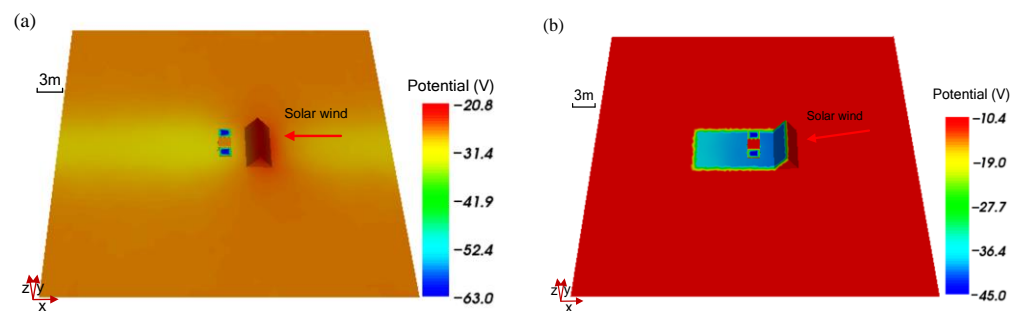


Figure 9. Charging potential of lunar rovers in a shadow at the solar altitude angle of 1° (a) and 10° (b).

For the entire simulated domain, the potential of the upper boundary at 80 m height is zero under both solar altitude angles, which meets the boundary conditions. As shown in Figure 10a, the difference is that at a solar altitude angle of 1° , the plasma potential distribution near the lunar surface is relatively uniform, with only a small area of low plasma potential at 7-m downwind of the lunar rover. At a solar altitude angle of 10° (Figure 10b), there is a larger decrease in the plasma potential between the lunar rover and the bulge, which extends to the upper space with a radius of 5 m. It is worth noting that there appears to be a relatively large potential surrounding the rover.

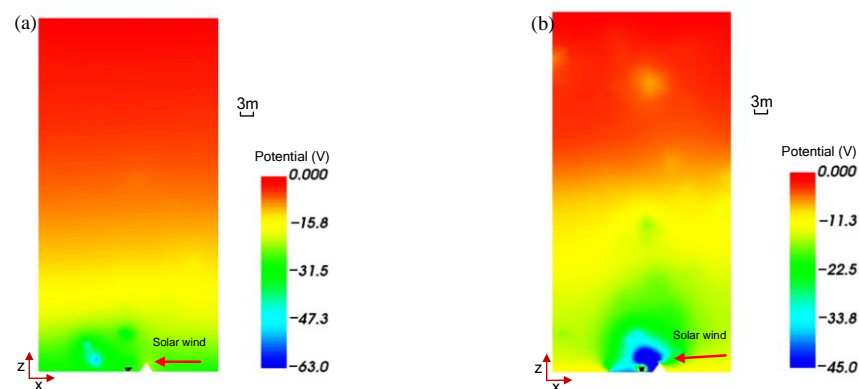


Figure 10. Charging potential of the near-surface influenced by a bulge with the solar altitude angle of 1° (a) and 10° (b).

The results of the bulge-shadowing effect can apply to the shielding of the lander and rover by other positively elevated terrains with similar magnitudes, such as boulders, and even the shielding of the rover by the lander. It is important to emphasize that the above bulge-shadowing effect is different from the wake effect of large-scale terrains such as

mountains and deep large craters. On the windward surface of the large-scale topography, the solar wind plasma is absorbed, while the plasma voids are formed on the leeward side of these obstacles. Due to the difference in velocity and deflection angle between electrons and ions, the electron-rich plasma regions are identified as “electron cloud” areas with extremely negative potential. However, no “electron cloud” area is formed in the bulge shadow region, since ions can be deflected and reach this region.

4.3. Lunar Rover Charging near an Impact Crater

On the Moon, the widely distributed craters will also have an impact on the local/regional charging environment and the rover. We consider two situations that a rover explores near a meter-scale crater (hemispherical model with a diameter of 5 m and rim height of 0.25 m): (i) the rover charging in the upwind direction of the crater, and (ii) the rover charging in the downwind direction of the crater. Here, the solar altitude angle is considered as 1° for a general situation of the future landing area. Assuming the rover is investigating and/or sampling 2.5-m away from the crater rim, the simulation domain is increased to $50\text{ m} \times 50\text{ m} \times 80\text{ m}$. In the first situation, the overall charging potential of the surface is relatively high with an average value of -24.21 V (Figure 11a). There is an obvious low potential area near the upwind side of the rover, which is charged to the minimum value of -29.3 V . Additionally, an apparent low potential area is formed in the leeward side of the crater due to the shadowing effect of the crater rim. In the second situation, a similar but lower potential area with a radius of $\sim 4\text{ m}$ is formed near the rover on the leeward side of the crater (Figure 11b). The lowest potential (-31.6 V) area in this case occurs on the upwind side of the rover. Comparing the two situations, the rover will be charged to a lower negative potential when in situ investigating and/or sampling on the leeward side of the crater.

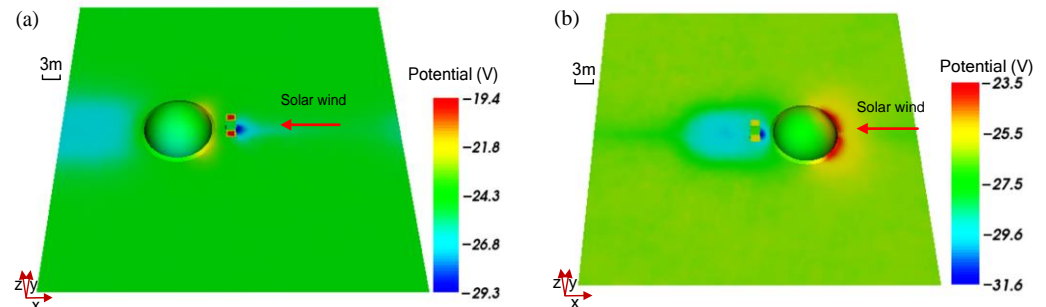


Figure 11. Rover charging potentials on the windward (a) and leeward (b) sides of the impact crater with a solar altitude angle of 1° .

It is also interesting to compare the plasma potential distribution of the near-surface space when the rover traverses at different positions around the crater. As shown in Figure 12a,b, locating the rover in the downwind direction of the crater induces a significantly higher altitude of low-potential plasma than locating the rover in the upwind direction of the crater. In addition, the rover endures a much lower potential of the near-surface on the downwind side of the crater (Figure 12b). This means that a favorable traversing and sampling site for lunar polar exploration such as CE-7 would be located in the upwind direction of the crater, where the solar wind has a minimal impact on the charging process of the lunar rover.

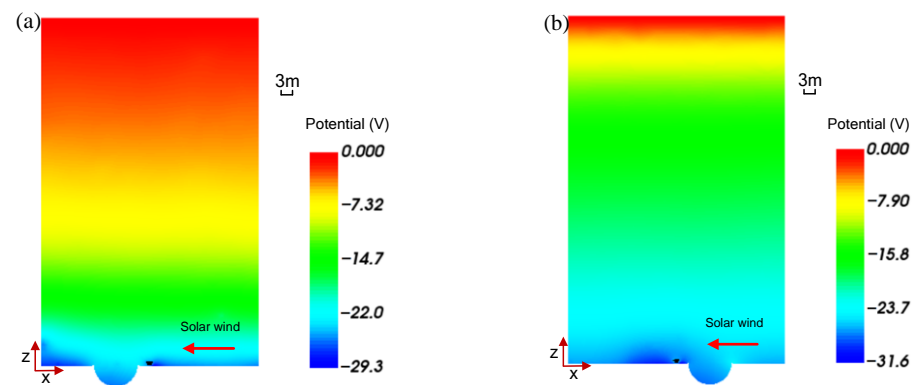


Figure 12. The distribution of plasma potential near the impact crater when the solar altitude angle is 1° , and the rover is located in the upwind (a) and downwind (b) directions of the impact crater.

5. Discussion

Lunar polar exploration is an interesting and exciting mission that would extend our knowledge with the first touch of the Moon's polar region. However, the extreme dynamic lighting conditions and electric field at the cratered polar regions make landing-site selection crucial. The rover spends most of its time in the sunlight since the illumination rate of the selected landing sites within the regions of interest should be maximized to ensure energy supply.

However, unlike the low latitude regions, the rover could easily be obscured by the lander or meter-sized boulders because of the extremely low solar altitude angle, and then a complex plasma environment is formed. In this work, using SPIS, we analyzed how the rover changes the surrounding electric-field environment. The results confirmed that the electric-field environment that the rover may face in the lunar polar regions will be influenced by the illumination conditions, the terrain, and the rover itself. Their influence on the space plasma can be extended to 15–30-m above the lunar surface. This means that the detection equipment still could not avoid the impact of the lander, rover, terrain, and illumination conditions, even if mounted at a height of several meters above the lunar surface such as 1.9 m (in situ dust detector of CE-3) or 2.0 m (in situ dust detector of CE-5).

In addition, the ubiquitous craters and even the rover itself also have a significant influence on the plasma environment around the rover, which means that the nearly dynamic electric field surrounding the rover may increase the risk to the electronic control system of the rover. Therefore, we propose that rover path planning including in situ investigation and sample drilling should follow the real-time illumination and electric-field conditions by combining the real-time Sun–Earth–Moon positions, solar wind plasma conditions, and the local terrain of the lunar surface. That is, a detailed 3D model of the rover exploring the target region should be simulated, by SPIS software (Version 5.2.4) for example, before the launch of the CE-7 and during the mission operation. Therefore, software capable of robust real-time path planning for the rover [32] can be developed for designed multipoint wide-area and longitudinal sampling modes.

In summary, the ubiquitous positive (such as the lander or boulders) and negative (such as craters) terrains in polar regions cause a complex electric field due to variations of solar-wind incidence. Then, the charged dust particles are raised by the electric field. Thus, dust particles will adhere to the rover, which is hazardous to the rover during the sampling mission. In this study, we propose that the rover traversing and/or sampling on the windward side of the crater and bulge could minimize the risk of the charging effect. However, the actual terrain could make the situation complex. Therefore, it is necessary to integrate a real-time charging model into the robust SPIS software (Version 5.2.4) for path planning.

It is worth noting that the material of the rover also plays an important role in charging features that are induced by solar radiation and solar-wind implantation. Compared to the

low/mid-latitude area exploration, the rover's long-term exposure to the variable solar radiation and solar wind may result in a continuous charging effect. This may increase the risk to the rover's electrical and mechanical systems. Therefore, a detailed simulation of the interaction between different aerospace materials and the polar environment should be studied, and the induced electric field and adhered dust should also be characterized. Furthermore, ground experiments of aerospace materials exposed to the simulated polar environment would provide more constrained parameters to SPIS simulations.

6. Conclusions

Chang'E-7 will target the lunar south pole in 2026. One of the mission elements, the rover, will drill lunar samples in sunlit areas for in situ investigation. In this study, we present detailed engineering constraints of the polar environment in a 15×15 km area, which might be a potential landing area. We found that the complex terrain in terms of slope affects the local solar altitude angle, which influences the amount of solar energy received by the rover. The simulation of real-time illumination indicates that high elevations of the topography such as crater rims and connecting ridges have a higher illumination rate within the study area. Two potential exploration regions, PLS 1 (137.14° W, 89.44° S) and PLS 2 (135.22° W, 90.00° S), can be continuously illuminated for more than 90 and 67 days in 2026, to give an example. PLS 1 and 2 could be favorable targets for landing-site selection and rover traversing planning. The electric field in a sunlit area presents a small potential in absolute value compared to the shadowed areas.

Considering the complex terrain of the exploration area at a meter scale, we created a 3D model of the rover with different material components by employing the Spacecraft Plasma Interaction Software (Version 5.2.4). The result showed that the rover can be charged to different magnitudes when traversing and/or sampling on a flat surface, in a shadow, and near a meter-scale crater. We also find that a favorable traversing and/or sampling site of the rover for future polar exploration is in the upwind direction of a bulge and crater which has a minimum charging effect.

Our results help to assess the environmental challenges of the rover for future explorations on flat surfaces or near positive or negative terrain. In future work, a higher resolution of the surface terrain will be integrated into the SPIS model. Thus, an improved 3D rover model interacting with the polar environment under real-time illumination and the electric field will be created. The surface traversing and/or sampling plan for in situ geological investigation will be guided and constrained by the simulations. This will help us to increase the utilization of solar energy and to decrease the risks of the hazardous environment for rover exploration.

Author Contributions: Conceptualization, H.G. and G.W.; methodology, G.W. and C.Z.; software, G.W. and C.Z.; validation, H.G., G.W. and C.Z.; formal analysis, X.L.; investigation, G.X.; resources, X.Z.; data curation, J.S.; writing—original draft preparation, H.G.; writing—review and editing, H.G. and G.W.; visualization, C.Z.; supervision, G.X.; project administration, X.Z. and J.S.; funding acquisition, H.G. All authors have read and agreed to the published version of the manuscript.

Funding: This research was funded by the National Key Research and Development Program of China (2022YFF0711400), the National Natural Science Foundation of China (42241154, 41903058, 12075108), the Frontier Science Research Program of Deep Space Exploration Laboratory (2022-QYKYJH-HXYF-023), the Science and Technology Program of Guizhou Province (QKHJC-ZK[2023]-131, QKHJC-ZK[2023]-476), and the open-source software provided by the Spacecraft Plasma Interactions Network in Europe (SPINE).

Data Availability Statement: The data presented in this study are available on request from two corresponding authors.

Conflicts of Interest: The authors declare no conflict of interest.

References

1. Colaprete, A.; Schultz, P.; Heldmann, J.; Wooden, D.; Shirley, M.; Ennico, K.; Hermalyn, B.; Marshall, W.; Ricco, A.; Elphic, R.C. Detection of water in the LCROSS ejecta plume. *Science* **2010**, *330*, 463. [\[CrossRef\]](#)
2. Li, S.; Lucey, P.G.; Milliken, R.E.; Hayne, P.O.; Fisher, E.; Williams, J.-P.; Hurley, D.M.; Elphic, R.C. Direct evidence of surface exposed water ice in the lunar polar regions. *Proc. Natl. Acad. Sci. USA* **2018**, *115*, 8907. [\[CrossRef\]](#)
3. Kereszturi, A. Polar Ice on the Moon. In *Encyclopedia of Lunar Science*; Cudnik, B., Ed.; Springer: Cham, Switzerland, 2022. [\[CrossRef\]](#)
4. Bussey, D.B.J.; Spudis, P.D.; Robinson, M.S. Illumination conditions at the lunar South Pole. *Geophys. Res. Lett.* **1999**, *26*, 1187. [\[CrossRef\]](#)
5. Mazarico, E.; Neumann, G.A.; Smith, D.E.; Zuber, M.T.; Torrence, M.H. Illumination conditions of the lunar polar regions using LOLA topography. *Icarus* **2011**, *211*, 1066. [\[CrossRef\]](#)
6. De Rosa, D.; Bussey, B.; Cahill, J.T.; Lutz, T.; Crawford, I.A.; Hackwill, T.; van Gasselt, S.; Neukum, G.; Witte, L.; McGovern, A. Characterisation of potential landing sites for the European Space Agency's Lunar Lander project. *Planet. Space Sci.* **2012**, *74*, 224. [\[CrossRef\]](#)
7. Caluk, N.; Aziznamini, A. Introduction to the concept of modular blocks for lunar infrastructure. *Acta Astronaut.* **2023**, *207*, 153–166. [\[CrossRef\]](#)
8. Colaprete, A.; Andrews, D.; Bluethmann, W.; Elphic, R.C.; Bussey, B.; Trimble, J.; Zacny, K.; Captain, J.E. An overview of the Volatiles Investigating Polar Exploration Rover (VIPER) mission. In Proceedings of the AGU Fall Meeting, San Francisco, CA, USA, 9–13 December 2019; p. P34B-03.
9. Smith, K.E.; Colaprete, A.; Lim, D.; Andrews, D. The VIPER Mission, a Resource-Mapping Mission on Another Celestial Body. In Proceedings of the Space Resources Roundtable XXII Meeting, Golden, CO, USA, 7–10 June 2022.
10. Ohtake, M.; Karouji, Y.; Ishihara, Y.; Nomura, R.; Inoue, H.; Shiraiishi, H.; Mizuno, H.; Hoshino, T.; Asoh, D. Current Status of the Planned Lunar Polar Exploration Mission Jointly Studied by India and Japan. In Proceedings of the 52nd Lunar and Planetary Science Conference, Virtual Conference, 15–19 March 2021; LPI Contribution No. 2548, id 1840.
11. Hoshino, T.; Wakabayashi, S.; Ohtake, M.; Karouji, Y.; Hayashi, T.; Morimoto, H.; Shiraiishi, H.; Shimada, T.; Hashimoto, T.; Inoue, H. Lunar polar exploration mission for water prospection-JAXA's current status of joint study with ISRO. *Acta Astronaut.* **2020**, *176*, 52. [\[CrossRef\]](#)
12. Zou, Y.; Liu, Y.; Jia, Y. Overview of China's Upcoming Chang'E Series and the Scientific Objectives and Payloads for Chang'E 7 Mission. In Proceedings of the 51st Annual Lunar and Planetary Science Conference, Woodlands, TX, USA, 16–20 March 2020; No. 2326. p. 1755.
13. Wei, G.; Li, X.; Zhang, W.; Tian, Y.; Jiang, S.; Wang, C.; Ma, J. Illumination conditions near the Moon's south pole: Implication for a concept design of China's Chang'E-7 lunar polar exploration. *Acta Astronaut.* **2023**, *208*, 74–81. [\[CrossRef\]](#)
14. Farrell, W.; Stubbs, T.; Halekas, J.; Killen, R.; Delory, G.; Collier, M.; Vondrak, R. Anticipated electrical environment within permanently shadowed lunar craters. *J. Geophys. Res. Planets* **2010**, *115*, E3. [\[CrossRef\]](#)
15. Zakharov, A.; Zelenyi, L.; Popel', S. Lunar dust: Properties and potential hazards. *Sol. Syst. Res.* **2020**, *54*, 455. [\[CrossRef\]](#)
16. Wagner, S. *The Apollo Experience Lessons Learned for Constellation Lunar Dust Management*; NASA Johnson Space Center: Houston, TX, USA, 2006; NASA/TP-2006-213726.
17. Gaier, J.R. *The Effects of Lunar Dust on EVA Systems during the Apollo Missions*; NASA Glenn Research Center: Cleveland, OH, USA, 2007; NASA/TM-2005-213610.
18. Zimmerman, M.; Farrell, W.; Stubbs, T.; Halekas, J.; Jackson, T. Solar wind access to lunar polar craters: Feedback between surface charging and plasma expansion. *Geophys. Res. Lett.* **2011**, *38*, 19. [\[CrossRef\]](#)
19. Farrell, W.M.; Stubbs, T.; Vondrak, R.; Delory, G.; Halekas, J. Complex electric fields near the lunar terminator: The near-surface wake and accelerated dust. *Geophys. Res. Lett.* **2007**, *34*, 14. [\[CrossRef\]](#)
20. Xie, L.; Zhang, X.; Li, L.; Zhou, B.; Zhang, Y.; Yan, Q.; Feng, Y.; Guo, D.; Yu, S. Lunar dust fountain observed near twilight craters. *Geophys. Res. Lett.* **2020**, *47*, e2020GL089593. [\[CrossRef\]](#)
21. Zimmerman, M.I.; Jackson, T.; Farrell, W.; Stubbs, T. Plasma wake simulations and object charging in a shadowed lunar crater during a solar storm. *J. Geophys. Res. Planets* **2012**, *117*, E10. [\[CrossRef\]](#)
22. Zimmerman, M.; Farrell, W.; Stubbs, T. Recursive plasma wake formation on the Moon and its effect on polar volatiles. *Icarus* **2013**, *226*, 992. [\[CrossRef\]](#)
23. Rhodes, D.J.; Farrell, W. Steady-State Solution of a Solar Wind-Generated Electron Cloud in a Lunar Crater. *J. Geophys. Res. Space Phys.* **2019**, *124*, 4983. [\[CrossRef\]](#)
24. Mishra, S.K. A Discussion on Electrostatics within Permanently Shadowed Craters on Moon. *Plasma Phys. Rep.* **2023**, *49*, 23–28. [\[CrossRef\]](#)
25. Li, D.; Wang, Y.; Zhang, H.; Zhuang, J.; Wang, X.; Wang, Y.; Yang, S.; Sun, Z.; Wang, X.; Chen, L. In situ measurements of lunar dust at the Chang'E-3 landing site in the northern Mare Imbrium. *J. Geophys. Res. Planets* **2019**, *124*, 2168. [\[CrossRef\]](#)
26. Zhuang, J.; Kong, F.; Gu, Z.; Li, D.; Wang, Y.; Li, C.; Chen, L.; Wang, Y.; Miao, Y.; Li, X. A design of in-situ detector of charged lunar dust (DCLD). *Sens. Actuators A Phys.* **2021**, *320*, 112564. [\[CrossRef\]](#)

27. Hess, S.; Sarraïlh, P.; Matéo-Vélez, J.-C.; Jeanty-Ruard, B.; Cipriani, F.; Forest, J.; Hilgers, A.; Honary, F.; Thiébaud, B.; Marple, S. New SPIS capabilities to simulate dust electrostatic charging, transport, and contamination of lunar probes. *IEEE Trans. Plasma Sci.* **2015**, *43*, 2799. [[CrossRef](#)]
28. Xia, Q.; Cai, M.-H.; Xu, L.-L.; Han, R.-L.; Yang, T.; Han, J.-W. Distribution of charged lunar dust in the south polar region of the moon. *Chin. Phys. B* **2022**, *31*, 045201. [[CrossRef](#)]
29. Bernhardt, H.; Robinson, M.S.; Boyd, A.K. Geomorphic map and science target identification on the Shackleton-de Gerlache ridge. *Icarus* **2022**, *379*, 114963. [[CrossRef](#)]
30. Kereszturi, A.; Tomka, R.; Gläser, P.A.; Pal, B.D.; Steinmann, V.; Warren, T. Characteristics of de Gerlache crater, site of girlands and slope exposed ice in a lunar polar depression. *Icarus* **2022**, *388*, 115231. [[CrossRef](#)]
31. Vaverka, J.; Richterová, I.; Pavlů, J.; Šafránková, J.; Němeček, Z. Lunar surface and dust grain potentials during the earth's magnetosphere crossing. *Astrophys. J.* **2016**, *825*, 133. [[CrossRef](#)]
32. Kuang, B.; Gu, C.; Rana, Z.A.; Zhao, Y.; Sun, S.; Nnabuife, S.G. Semantic Terrain Segmentation in the Navigation Vision of Planetary Rovers—A Systematic Literature Review. *Sensors* **2022**, *22*, 8393. [[CrossRef](#)] [[PubMed](#)]

Disclaimer/Publisher's Note: The statements, opinions and data contained in all publications are solely those of the individual author(s) and contributor(s) and not of MDPI and/or the editor(s). MDPI and/or the editor(s) disclaim responsibility for any injury to people or property resulting from any ideas, methods, instructions or products referred to in the content.